Stepwise assembly of the active site of [NiFe]-hydrogenase

Giorgio Caserta,[1,6*] Sven Hartmann,[1,6] Casey van Stappen,[2] Chara Karafoulidi-Retsou,[1] Christian Lorent,[1] Stefan Yelin,[3] Matthias Keck,[3] Janna Schoknecht,[1] Ilya Sergueev,[4] Yoshitaka Yoda,[5] Peter Hildebrandt,[1] Christian Limberg,[3] Serena DeBeer,[2] Ingo Zebger,[1] Stefan Frielingsdorf,[1*] and Oliver Lenz[1*]

[1] Institut für Chemie, Technische Universität Berlin, Straße des 17. Juni 135, 10623 Berlin, Germany

[2] Department of Inorganic Spectroscopy, Max Planck Institute for Chemical Energy Conversion, Stiftstraße 34-36, 45470 Mülheim an der Ruhr, Germany

[3] Department of Chemistry, Humboldt-Universität zu Berlin, Brook-Taylor-Straße 2, 12489 Berlin, Germany

[4] Deutsches Elektronen-Synchrotron, Notkestraße 85, 22607 Hamburg, Germany

[5] Japan Synchrotron Radiation Research Institute (JASRI), SPring-8, 1-1-1 Kouto, Sayo-gun, Hyogo 679-5198, Japan

[6] These authors contributed equally: Giorgio Caserta, Sven Hartmann

[*]emails: giorgio.caserta@tu-berlin.de; stefan.frielingsdorf@tu-berlin.de; oliver.lenz@tu-berlin.de

Abstract

[NiFe]-hydrogenases are biotechnologically relevant enzymes catalyzing the reversible splitting of H_2 into 2 e^- and 2 H^+ under ambient conditions. Catalysis takes place at the heterobimetallic $NiFe(CN)_2(CO)$ center, whose multistep biosynthesis involves careful handling of two transition metals as well as potentially harmful CO and CN^- molecules. Here, we investigated the sequential assembly of the [NiFe]-cofactor, previously based on primarily indirect evidence, using four different purified maturation intermediates of the catalytic subunit, HoxG, of the O_2-tolerant membrane-bound hydrogenase from *Cupriavidus necator*. These included the cofactor-free apo-HoxG, a nickel-free version carrying only the $Fe(CN)_2(CO)$ fragment, a precursor that contained all cofactor components but remained redox-inactive, and the fully mature HoxG. Through biochemical analyses combined with comprehensive spectroscopic investigation using infrared, electronic paramagnetic resonance, Mössbauer, X-ray absorption, and nuclear resonance vibrational spectroscopies, we obtained detailed insight into the sophisticated maturation process of [NiFe]-hydrogenase.

Main

Hydrogenases employ complex metal cofactors for the reversible conversion of H_2 into protons and electrons.[1] According to their active site metal content, they are grouped into the three phylogenetically independent classes of [NiFe]-, [FeFe]- and [Fe]-hydrogenases.[2,3] The metal centers of [FeFe]- and [Fe]-hydrogenases are covalently bound to the protein via a single cysteine residue, and their assembly takes place under strictly anaerobic conditions involving, among others, dedicated radical S-adenosylmethionine (radical-SAM) enzymes.[4,5] In contrast, the biosynthetic machinery of the heterobimetallic cofactor of [NiFe]-hydrogenases operates independently of radical-SAM enzymes[6–8] and, in some cases, even under aerobic conditions.[9]

In the present study, we dissected the multistep biosynthesis process of the catalytic center of [NiFe]-hydrogenases by isolating and analyzing four different maturation intermediates (**Fig. 1**). The basic module of [NiFe]-hydrogenases is composed of a large subunit that houses the catalytic metal center and a small subunit that contains an electron relay consisting of one to three Fe-S clusters.[8–10] The active site nickel ion is covalently bound to the protein scaffold via four conserved cysteine residues (Cys1-4 in **Fig. 1**, Cys3 is replaced with a selenocysteine residue in case of [NiFeSe]-hydrogenase[11]). Two of these cysteines (Cys2 and Cys4) serve as bridging ligands coordinating also the iron ion, which is additionally ligated by two cyanide ions and one carbon monoxide molecule.[12] A free coordination site is located between the two metals, which, depending on the redox conditions, either remains empty or can accommodate a bridging hydride or a hydroxy ligand.[13,14]

Biosynthesis of the $NiFe(CN)_2(CO)$ cofactor requires an intriguing protein machinery comprising at least six accessory proteins termed HypA-F.[6,7,15] According to the current model, the $Fe(CN)_2(CO)$ moiety of the cofactor is assembled on a complex consisting of the auxiliary proteins HypC and HypD (**Fig. 1**).[16,17] The CN^- ligands of this iron unit are synthesized by HypE and HypF proteins using carbamoyl phosphate as substrate.[18] The biosynthesis of the CO from formyl-tetrahydrofolate under aerobic conditions has been recently elucidated,[19,20] whereas the pathway responsible for CO ligand production under anaerobic conditions remains elusive.[7] The completed $Fe(CN)_2(CO)$ fragment is assumed to be transferred from HypC(D) to the apo-form of the large subunit (**Fig. 1**).[16,21–23] In the next step, the nickel ion is inserted with the aid of the maturases HypA and HypB.[7,24] The vast majority of [NiFe]-hydrogenase subunit precursors carries a C-terminal extension, which is cleaved by a hydrogenase-specific endopeptidase after insertion of the nickel into the active site cavity.[21,25,26] Cleavage of the C-terminal extension triggers association of the small and large subunit, yielding a fully active [NiFe]-hydrogenase (**Fig. 1**).

Although the structures of all Hyp maturases have been elucidated,[1,15] the current maturation model is still based mainly on genetic and biochemical studies performed on non-purified large subunit intermediates.[6,7,21,27-28] Thus, the actual cofactor content and the structure of several intermediates is not yet determined.

Here, we employed the large subunit HoxG of the membrane-bound hydrogenase (MBH) from *Cupriavidus necator* (formerly *Ralstonia eutropha*) as a model system for an in-depth investigation of the sequential biosynthesis process of the $NiFe(CN)_2(CO)$ cofactor in the active site cavity. Consisting of the large subunit HoxG and the small subunit HoxK, the MBH of *C. necator* belongs to the biotechnologically relevant subclass of O_2-tolerant [NiFe]-hydrogenases,[29-30] whose members are synthesized and perform catalysis under aerobic conditions.[9,31] Although specific auxiliary proteins come into play for the biosynthesis of *C. necator* MBH, the core maturation apparatus consists of the Hyp proteins mentioned above.[9] By disabling individual Hyp functions, we interrupted MBH maturation at various stages and purified the corresponding HoxG intermediates shown in **Fig. 1**. All intermediates were analyzed for metal content and spectroscopically characterized by infrared (IR), electron paramagnetic resonance (EPR), Mössbauer, X-ray absorption and nuclear resonance vibrational spectroscopies (XAS and NRVS, respectively). The corresponding results revealed important details about the stepwise assembly of the [NiFe]-hydrogenase active site.

Results

MBH large subunits arrested in distinct maturation stages

In a previous investigation we showed that the MBH large subunit can be isolated via a Strep-tag that had been attached to the C-terminal extension of HoxG.[32] This preHoxG version ($preHoxG^S$) contained the [NiFe]-active site only in sub-stoichiometric amounts (approx. 20 %). Recent studies of the isolated large subunit HoxC of the regulatory [NiFe]-hydrogenase (RH) of *C. necator*, however, revealed almost stoichiometric loading with the inorganic $NiFe(CN)_2(CO)$ unit upon isolation via an N-terminal Strep-tag.[33] To achieve full cofactor loading, we designed an N-terminally Strep-tagged HoxG, and the corresponding gene construct was put under control of the MBH promoter. The resulting plasmid, pGC50, was transferred to different *C. necator* mutant strains (Supplementary Information, **Supplementary Table 1**) to isolate HoxG maturation intermediates.

The isolation of the individual maturation intermediates depicted in **Fig. 1** was based on the following assumptions. i) A *C. necator* strain deleted for the maturase gene *hypD* is incapable of mediating the proposed initial step of cofactor insertion, i.e. the assembly of the

$Fe(CN)_2(CO)$ fragment on the HypCD complex and its transfer to the apo-form of the large subunit. Thus, this strain background should allow the isolation of apo-HoxG (named preHoxG$^{\Delta FeNi}$) carrying the C-terminal extension (indicated by the prefix "pre") but lacking the $NiFe(CN)_2(CO)$ cofactor. ii) preHoxG devoid of just the nickel ion (preHoxG$^{\Delta Ni}$) can be purified from a mutant lacking the appropriate nickel processing machinery, i.e. the nickel permease HoxN[34] and the specific nickel-insertion proteins HypA and HypB. iii) Deletion in the endopeptidase gene *hoxM*[35] allows for isolation of preHoxG containing both the $NiFe(CN)_2(CO)$ cofactor and the C-terminal extension. iv) Finally, the isolated, fully mature HoxG subunit (mHoxG) can be obtained from a mutant strain in which the gene encoding the MBH small subunit HoxK has been genetically deleted.[32]

The resulting transconjugants (**Supplementary Table 1**) were grown in minimal media, and Strep-tagged HoxG versions were purified as described in Methods. Protein purity was confirmed by SDS-PAGE and immunological analyses (**Figs. 2a**, **b**). All variants of HoxG containing the C-terminal extension of 15 amino acid residues (ca. 1.6 kDa) exhibit slightly lower mobility in the SDS-PAGE gel than those lacking this extension. The highest mobility was observed for HoxG of the MBH control, which contains neither the C-terminal extension nor an N-terminal Strep-tag (ca. 1.2 kDa). Notably, the small subunit HoxK was not co-purified with any of the preHoxG intermediates, despite the presence of the *hoxK* gene in the genetic backgrounds employed (**Fig. 2b**). The mHoxG variant did not interact with HoxK because the *hoxK* gene was deleted. Furthermore, both preHoxG$^{\Delta FeNi}$ and preHoxG$^{\Delta Ni}$ still contained the C-terminal extension despite the presence of the endopeptidase HoxM. Thus, proteolytic processing occurs only after $Fe(CN)_2(CO)$ and Ni have both been inserted into the large subunit. This has been proposed previously,[21,26,36] but direct experimental evidence obtained with purified intermediates has so far been lacking.

$Fe(CN)_2(CO)$ fragment incorporation precedes Ni insertion

To verify our assumptions on the cofactor loading of the HoxG intermediates, we analyzed the metal content of the purified proteins by inductively coupled plasma optical emission spectroscopy (ICP-OES). ICP-OES revealed the presence of ~20 % of iron loading in preHoxG$^{\Delta FeNi}$ and near to stoichiometric iron content in all the other samples (**Table 1**). As expected, significant amounts of nickel were only detected in preHoxG (77 %) and mHoxG (75 %). To examine whether the iron ions were equipped with the typical CO and CN^- ligands, we recorded IR spectra of the four intermediates (**Fig. 2c**). The preHoxG$^{\Delta FeNi}$ sample displayed trace signals in the region of 2150 – 1800 cm^{-1}, consistent with less than 1% cofactor loading

(**Supplementary Fig. 1**). All other intermediates, by contrast, exhibited prominent CO and CN stretching vibrations (**Fig. 2c**, **Supplementary Table 2**), in line with the Fe (and Ni) content (**Table 1**). For the preHoxG$^{\Delta Ni}$ intermediate, we detected predominant CO bands at 1949 and 1962 cm^{-1} in addition to a smaller high-frequency absorption at 1997 cm^{-1}. CN bands appeared at 2072 and 2092 cm^{-1}. The appearance of rather broad signals in preHoxG$^{\Delta Ni}$ suggests a certain degree of structural flexibility. Presumably, these bands originate from a slight variations in coordination of the Fe(CN)$_2$(CO) fragment due to the absence of the Ni ion (**Fig. 1**).[37]

The IR spectrum of preHoxG shows a dominant CO band at 1953 cm^{-1} and CN absorptions at 2066 and 2076 cm^{-1}, with a minor contribution at 2090 cm^{-1} (**Fig. 2c**, **Supplementary Table 2**). The spectrum is virtually identical to that of the previously characterized preHoxG version carrying a Strep-tag at the end of the C-terminal extension (preHoxG^{S}).[32] Notably, the C-terminally tagged version showed a significantly lower NiFe(CN)$_2$(CO) cofactor loading (**Supplementary Fig. 2**). Thus, the Strep-tag addition to the C-terminal extension clearly has a negative effect on the insertion of the inorganic cofactor.

Fully mature mHoxG exhibits main CO absorptions at 1929 and 1939 cm^{-1} in addition to a broad shoulder at 1953 cm^{-1}, while CN stretching vibrations occurred at 2057 and 2070 cm^{-1}, with an additional minor band at 2090 cm^{-1}. The small contributions at 1953 cm^{-1} and 2090 cm^{-1} reflect remnants (ca. 20 %) of preHoxG molecules in the mHoxG sample as substantiated by NRVS and Mössbauer analysis (see below). Nevertheless, the IR spectra of preHoxG and mHoxG differ significantly, suggesting that the cleavage of the C-terminal extension has a great impact on the structure of the catalytic center. In summary, the metal content and IR data agree with the presumed cofactor compositions of the HoxG intermediates. In addition, the results clearly demonstrate that Fe(CN)$_2$(CO) incorporation precedes Ni insertion.

The C-terminal extension improves cofactor incorporation

The presence of the C-terminal extension is not obligatory for NiFe(CN)$_2$(CO) cofactor insertion into apo-HoxG, but seems to markedly improve the fidelity of maturation, resulting in a higher amount of mature and catalytically active MBH.[25] To investigate the impact of the C-terminal extension on the cofactor loading of the HoxG intermediates, we constructed two additional processed (proc) versions, procHoxG$^{\Delta Ni}$ and procHoxG, in which the C-terminal extension was removed by genetic engineering (**Supplementary Table 1**). The HoxG versions were purified, analyzed by SDS-PAGE and immunoblots (**Figs. 2a**, **b**), and subsequently compared to their counterparts preHoxG$^{\Delta Ni}$ and mHoxG (**Supplementary Fig. 3**).

The IR spectra show CO and CN stretching vibrations for both intermediates, confirming that they undergo metal center insertion even without the C-terminal extension (**Supplementary discussion 1**). In fact, the IR spectrum of procHoxG showed features almost identical to those of proteolytically processed mHoxG in terms of peak positions (**Supplementary Fig. 3a,b**), indicating that both the $Fe(CN)_2(CO)$ moiety and nickel are present in procHoxG. This is consistent with our previous observation that procHoxG and the small subunit HoxK form a fully functional MBH version with native catalytic activity.[25] One rather minor difference is the absence of CO and CN absorptions at 1953 cm^{-1} and 2090 cm^{-1} in the procHoxG spectrum, supporting their assignment to a small fraction of unprocessed molecules in the mHoxG fraction (see above and **Fig. 2c**). The absence of the band at 1953 cm^{-1} in procHoxG, however, uncovered a minor absorption at 1950 cm^{-1} of yet unknown origin (**Supplementary Fig. 3a**). In contrast to procHoxG and mHoxG, the IR spectra of procHoxG$^{\Delta Ni}$ and preHoxG$^{\Delta Ni}$ display larger differences. The preHoxG$^{\Delta Ni}$ intermediate exhibits an additional CO band at 1962 cm^{-1}, which was absent in the procHoxG$^{\Delta Ni}$ spectrum (**Supplementary Fig. 3c**,**d)**. This can be interpreted by an alternative coordination of the inorganic cofactor due to the presence of the C-terminal extension in preHoxG$^{\Delta Ni}$. Notably, the normalization of the active site CO/CN absorptions to intensity of the amide II band indicates a drastically lower occupancy of the genetically processed HoxG variants with the metal cofactors (**Supplementary Fig. 3**). Thus, albeit not essential for maturation, the C-terminal extension is required for full loading of the active site pocket with the respective metal cofactors.

Redox and spin states of the metal cofactor intermediates

The catalytic centers of as-isolated large subunits of [NiFe]-hydrogenases have shown to be EPR-silent, which has been interpreted with a Ni^{II}–Fe^{II} configuration of the active site metals.[32,33] To investigate the situation in the new HoxG intermediates, we determined the oxidation state of the active site metals in preHoxG$^{\Delta Ni}$, preHoxG, and mHoxG by EPR spectroscopy. The as-isolated samples contained minor signals of Fe^{III} species most likely unrelated to the hydrogenase active site (**Supplementary Fig. 4**), consistent with Fe/Ni ratios of 1.1 and 1.2 in preHoxG and mHoxG, respectively, and substoichiometric iron in preHoxG$^{\Delta FeNi}$ (**Table 1**). Therefore, the EPR data confirm a predominant diamagnetic Fe^{II} and, for the latter two intermediates, also a Ni^{II} configuration. To gain detailed information on the active site iron, we employed zero-field Mössbauer spectroscopy (**Fig. 3**) on the three ^{57}Fe-enriched intermediates, which were gel filtrated to limit Fe^{III} impurities. Resonance signals were simulated with different spectral components, and the resulting Mössbauer parameters are listed

in **Supplementary Table 3**. The main iron species in mHoxG (**Fig. 3a**, component 1) is characterized by an isomer shift of δ = 0.14 mm/s and a quadrupole splitting of ΔE_Q = 0.62 mm/s. These parameters are almost identical to those reported for the fully mature large subunit HoxC of the RH from *C. necator* (**Supplementary Table 3**) and in agreement with a 6-fold coordinated low-spin Fe^{II} ion.[33,38] Such 6-fold iron coordination is usually found in active site states bearing a bridging ligand (H^-, OH^-) in the vacant binding site.[1]

The Mössbauer spectrum of preHoxG is mainly characterized by a single iron species with an isomer shift of δ = 0.06 mm/s and a quadrupole splitting of ΔE_Q = 1.09 mm/s (**Fig. 3b**), which is again supportive of a low-spin Fe^{II} center. The larger ΔE_Q compared to that of mHoxG indicates a slightly more asymmetric coordination sphere, perhaps due to a coordination number of 5, and matches the IR analysis (**Fig. 2c**), which revealed a different arrangement/coordination of the $Fe^{II}(CN)_2(CO)$ unit in the two intermediates. Notably, the parameters of the main signal of preHoxG agree well with those of component 2 in the mHoxG spectrum (**Fig. 3a)**, suggesting the presence of ~ 20 % unprocessed preHoxG in the mHoxG preparation, which is also consistent with the IR data.

For the first time, we recorded a Mössbauer spectrum also of a nickel-free hydrogenase large subunit, $preHoxG^{\Delta Ni}$ (**Fig. 3c**). The signal was deconvoluted assuming two main iron species occurring with a partition of 78 % (δ_1 = 0.08 mm/s, ΔE_{Q1} = 1.02 mm/s) and 22 % (δ_2 = -0.08 mm/s, ΔE_{Q2} = 1.05 mm/s) (**Supplementary Table 3**). Both species are attributed to Fe^{II} low-spin centers, in line with the proposed sequence of maturation, i.e. the initial insertion of the low-spin $Fe^{II}(CN)_2(CO)$ fragment into the apo-protein.[22] The presence of two components reflects at least two different coordination patterns of the $Fe^{II}(CN)_2(CO)$ cofactor, which could be the result of alternatively coordinating cysteines (**Fig. 1**).[37] Notably, the Mössbauer parameters of the major iron species of $preHoxG^{\Delta Ni}$ and preHoxG are rather similar, suggesting that the presence or absence of the Ni ion has a smaller effect on the overall structure of the $Fe(CN)_2(CO)$ moiety than the presence or absence of the C-terminal extension.

NRVS spectra of the premature and mature HoxG intermediates

NRVS provides vibrational dynamics for Mössbauer-active nuclei, such as the active site iron when is present as ^{57}Fe isotope. Typical spectra of ^{57}Fe-labeled [NiFe]-hydrogenases comprise dominant Fe–S stretching and bending modes related to Fe-S clusters in the region of 100 – 420 cm^{-1},[39,40] and Fe–CO/CN bands in the region of 400 – 650 cm^{-1}.[39,41–42] The intermediates $preHoxG^{\Delta Ni}$, preHoxG and mHoxG are almost stoichiometrically loaded with iron (**Table 1**),

but devoid of Fe-S clusters thus enabling a selective probe of the vibrational modes of their active site iron (**Fig. 4a**).

According to the IR and Mössbauer data (**Figs. 2c** and **3**), preHoxG showed the highest homogeneity among the intermediates. This is consistent with the NRVS analysis, and therefore this intermediate is used as representative for describing the vibrational bands. The most intense bands were observed at 575 and 615 cm^{-1}, originating from modes of predominant Fe–CO stretching and Fe–C–O bending character.[39,41] The slightly weaker bands at 439, 493, and 508 cm^{-1} by contrast, originate from modes including both Fe–CO and Fe–CN coordinates, in line with recent results on the large subunit HoxC of the regulatory [NiFe]-hydrogenase.[39]
Because of the absence of Fe-S clusters, vibrational modes associated with the NiFe center were also detected in the low-frequency regime (**Fig. 4a**).[39,40]
The NRVS data of preHoxG$^{\Delta Ni}$ confirmed the presence of the $Fe(CN)_2(CO)$ fragment. The comparatively broad absorption bands suggest either a partial structural heterogeneity or higher flexibility of the $Fe(CN)_2(CO)$ unit, consistent with the results obtained from IR and Mössbauer spectroscopy. Nevertheless, the overall spectral pattern of preHoxG$^{\Delta Ni}$ in the region above 400 cm^{-1} displays striking similarity with that of preHoxG (**Fig. 4a**, red bars), suggesting a similar coordination of the iron fragment in the two intermediates.

In contrast, the NRVS data of preHoxG and mHoxG show marked differences, although both intermediates have the same metal content (**Table 1**). First, the two main Fe–CO bands at 615 and 575 cm^{-1} of preHoxG are shifted to 610 and 555 cm^{-1} in case of mHoxG. Among the possible origins for theses shifts, changes in the metal oxidation state can be excluded as both mHoxG and preHoxG appear diamagnetic, consistent with a Ni^{II}–Fe^{II} configuration. A different degree of protonation (at a nearby amino acid residue) of the two intermediates is also unlikely, as this would not cause significant spectral changes. Instead, compared to preHoxG, the mHoxG spectrum contains additional bands related to the active site. Among them are bands at 420 and 503 cm^{-1} (**Fig. 4a**, asterisks) located at positions similar to those reported for the RH large subunit HoxC in the Ni_r-S_I state, which is characterized by Ni^{II} and Fe^{II} ions bridged by a hydroxy group. (**Fig. 4b**).[39] Because of the good agreement of the experimental and computed spectra of HoxC with that of mHoxG, we assign the vibrational modes described above to the most prominent bridging OH displacements in the mHoxG active site, i.e., the Fe–OH (420 cm^{-1}) and Ni–OH stretching vibrations (503 cm^{-1}) (**Fig. 4a**,**b**).

In summary, our NRVS analysis indicates a similar coordination of the iron in preHoxG and preHoxG$^{\Delta Ni}$, with the latter having greater Fe-cofactor flexibility, and supports a different

coordination environment of the metal cofactor in the preHoxG and mHoxG intermediates, the latter hosting a bridging hydroxy ligand.

XAS-derived active site geometry and redox reactivity

Further details on the coordination environment of both the Ni and Fe ions in preHoxG and mHoxG were provided by K-edge X-ray absorption spectroscopy (**Supplementary discussion 2**). The XAS spectra, as well as the corresponding extended X-ray absorption fine structure (EXAFS) regions, are displayed in **Supplementary Figs. 8** and **9**. **Fig. 5** shows the Fourier-transformed EXAFS spectra of the Ni K- and Fe K-edges of mHoxG and preHoxG, respectively, including the best-fitting models (**Supplementary Tables 4** and **5**). For all models, the Ni–Fe distances were determined by simultaneous fitting of both Fe and Ni EXAFS data.

The Fe K-edge spectrum of mHoxG was best described by including 3 Fe–C scatterers (1.91 Å), accounting for the three diatomic ligands, 2 Fe–S (2.36 Å) scatterers, 6 Fe–C–N/O (3.07 Å) multiple scattering paths in addition to one Fe–Ni (2.82 Å) and one Fe–O (2.11 Å) scatterer (**Fig. 5a**). For the Ni K-edge data of mHoxG, the best fit revealed three discrete groups of Ni–S scatterers, including a 2-fold degenerate path at 2.23 Å, and two singly degenerate paths at 2.40 Å and 2.83 Å. The model also included 3 Ni–C (3.12 Å) scatterers (arising from C_β of cysteine) and one Ni–Fe (2.82 Å) scatterer in addition to a Ni–O (1.79 Å) scatterer with an occupancy between 0.5 (**Fig. 5b**) and 1.0, which agrees with the metal content of mHoxG (**Table 1**). The resulting active site model for mHoxG is depicted in **Fig. 5c** and is in good agreement with that computed for the RH large subunit HoxC.[39,40]

The best fit for the Fe K-edge spectrum of preHoxG (**Fig. 5d**) comprised 3 Fe–C scatterers split into a longer 2-fold degenerate path (Fe–C1, 1.93 Å, CN^- ligands) and a singly degenerate path (Fe–C2, 1.79 Å, CO ligand). This model also included 6 Fe–C–N/O (3.08 Å) multiple scattering paths, a 2-fold degenerate Fe–S path at 2.34 Å as well as a single Fe–Ni (2.77 Å) scatterer (**Fig. 5d**). For the Ni K-edge EXAFS of preHoxG, the best fit model was found to include 3 Ni–S1 scatterers at 2.22 Å, and one long-range scatterer, Ni–S3 (2.84 Å), in addition to 3 Ni–C (2.93 Å) scatterers and one Ni–Fe (2.77 Å) scatterer (**Fig. 5e**). The resulting model of the NiFe center in preHoxG is shown in **Fig. 5f**. In summary, both preHoxG and mHoxG exhibit a strikingly long Ni–S scatterer (2.77-2.82 Å) implying the fourth sulfur is outside of covalent bonding distance with Ni. Over-elongated bonds between the Ni^{II} and a bridging sulfur ligand have already been described for NiFe centers.[33,39,43] A major difference is the presence of an OH ligand bridging Ni and Fe, and this may result from only subtle

geometric changes of the active site that occur upon cleavage of the C-terminal extension of preHoxG. However, these changes result in a redox active site in mHoxG, while preHoxG remains inert. In fact, IR spectra of preHoxG and preHoxG$^{\Delta Ni}$ intermediates exhibited identical active site vibrations upon treatment with oxidizing (ferricyanide) and reducing (dithionite) agents and thus retained a (Ni^{II})Fe^{II} electronic configuration (**Supplementary discussion 3** and **Supplementary Fig. 10**). Conversely, the active site in mHoxG reacted with ferricyanide and dithionite yielding the paramagnetic Ni_r-B-like ($Ni^{III}Fe^{II}$) and the Ni_a-L ($Ni^{I}Fe^{II}$) species, respectively (**Supplementary Figs. 11** and **12**, **Supplementary Tables 2**, **3**, and **6**).

Discussion

In this study, we investigated the assembly process of the NiFe cofactor in the catalytic subunit of a [NiFe]-hydrogenase by isolating and characterizing so far postulated protein intermediates. To this end, we isolated four maturation intermediates of the MBH large subunit HoxG from *C. necator* (**Fig. 1**).

The presence of the maturases responsible for $Fe(CN)_2(CO)$ insertion and the concomitant absence of the nickel insertion machinery (HypA1, HypA2, HoxN) resulted in the formation of preHoxG$^{\Delta Ni}$ from the apo-protein preHoxG$^{\Delta FeNi}$. Spectroscopic characterization of the preHoxG$^{\Delta Ni}$ intermediate provided the first clear evidence that the $Fe(CN)_2(CO)$ fragment is delivered as an entire unit and that its incorporation into the apo-form of the large subunit precedes the Ni insertion. The latter assumption has been proposed earlier based on the observation that nickel is not incorporated into the large subunit precursor in the absence of an essential protein for the assembly of the $Fe(CN)_2(CO)$ fragment.[6,7,28] Notably, the CO and CN bands of preHoxG$^{\Delta Ni}$ have very similar frequencies as those reported for the HypCD complex (**Supplementary Fig. 13**), where the $Fe(CN)_2(CO)$ moiety is proposed to be coordinated by two cysteine residues.[15–17,44] According to the available [NiFe]-hydrogenase crystal structures, the $Fe(CN)_2(CO)$ fragment becomes attached to Cys2, and the specificity of insertion is most likely determined by the interaction of the CN/CO ligands with amino acids in the active site cavity.[29,45] Also consistent with all existing [NiFe]-hydrogenase crystal structures including that of the Ni-depleted [NiFeSe]-hydrogenase,[11] the $Fe(CN)_2(CO)$ moiety is coordinated by Cys2 and also by Cys4, which is located far from the active site in the metal-free precursor (**Fig. 1**).[37] However, at the current stage we cannot rule out alternative (cysteine) coordinations of the $Fe(CN)_2(CO)$ unit in preHoxG$^{\Delta Ni}$. Notably, Cys4 has been shown not to be required for nickel coordination in the large subunits of *E. coli* hydrogenase-3 as well as the soluble NAD^+-reducing hydrogenase and the regulatory hydrogenase of *C. necator*.[46–48] These observations

are consistent with our XAS data, indicating that Cys4 is beyond bond distance to the Ni ion in both preHoxG and mHoxG.

The isolation of HoxG from a *C. necator* strain lacking only the endopeptidase HoxM responsible for cleavage of the C-terminal extension yielded preHoxG, which contained nickel quantitatively in addition to the $Fe(CN)_2(CO)$ unit. Our Mössbauer and NRVS data revealed that the $Fe(CN)_2(CO)$ units in preHoxG$^{\Delta Ni}$ and preHoxG have a very similar coordination, with the iron fragment of preHoxG$^{\Delta Ni}$ displaying greater flexibility, presumably caused by the absence of nickel. Surprisingly, despite the same metal content, preHoxG and mHoxG show major differences in their spectroscopic IR patterns and Mössbauer parameters (**Figs. 2c** and **3**). NRVS and XAS analyses revealed a bridging OH^- ligand between the two heterometals in mHoxG (**Figs. 4b** and **5**). Interestingly, the XAS data also showed that, except for the OH^- group, the nature of the metal ion-coordinating ligands and the corresponding bond lengths of both preHoxG and mHoxG are very similar (**Figs. 5c,f**). This suggests that the cleavage of the C-terminus of preHoxG results in only subtle changes in the architecture of the active site. Nevertheless, these changes result in a redox-active catalytic center in mHoxG, as evident by significant changes in the IR and EPR spectra upon redox treatment (**Supplementary discussion 3** and **Supplementary Fig. 11**).

Based on our results, we draw the following important conclusions.

1. In the first step of cofactor assembly, the $Fe(CN)_2(CO)$ synthon of the [NiFe]-active site is incorporated as a whole unit into the apo large subunit and connected to Cys2. This step likely triggers the movement of Cys4 to the active site cavity, where it serves as the second binding site.

2. The nickel ion is being inserted in the second step and coordinated by Cys1, 2, and 3, while Cys4 remains at a non-bonding distance.

3. The C-terminal extension of the large subunit is not required for active site assembly but guarantees the full loading of the apo-large subunit with the [NiFe]-cofactor.

4. The “active site” of the premature intermediates, even that of preHoxG (fully equipped with the $NiFe(CN)_2(CO)$ site), remains redox-inactive.

5. The C-terminal extension is cleaved only after nickel insertion, and its removal leads to a restructuring of the active site with minor geometrical changes but accompanied by the incorporation of a hydroxy ligand between Ni and Fe.

6. Only the fully mature large subunit responds to redox treatment with oxidizing and reducing agents and is competent to form a complex with the small electron-transferring subunit to form an active [NiFe]-hydrogenase.

The biochemical and spectroscopic results reported here provide detailed insights into the assembly process of the [NiFe]-hydrogenase cofactor, which should be useful for the chemical synthesis of active site mimics. Moreover, the isolated intermediates serve as an ideal platform to study (semi-)artificial [NiFe]-hydrogenases equipped with chemically synthesized inorganic cofactors, as successfully demonstrated in the case of [FeFe]- and [Fe]-hydrogenases.[49,50] In particular, the intermediates preHoxG$^{\Delta FeNi}$ and preHoxG$^{\Delta Ni}$ could serve as receivers of synthetic iron complexes and Ni-replacing metals, respectively, and potentially reveal "chemzymes" with alternative catalytic functions.

Acknowledgements

G.C., S.H., O.L., I.Z., P.H. are grateful to the Einstein Foundation Berlin (grant number EVF-2016-277) for funding. This work was also supported by the Deutsche Forschungsgemeinschaft (DFG, German Research Foundation) through the PP 1927 “Iron Sulfur for Life” (project no. DE1877/1-1 (S.D.), 311062227 (O.L., I.Z.)) and the cluster of excellence “UniSysCat” under Germany´s Excellence Strategy-EXC2008/1-390540038. The authors are indebted for EU financial support (Article 38.1.2, GA) within the European Union’s Horizon 2020 research and innovation program under grant agreement no. 810856. C.V.S. and S.D. would like to thank the Max-Planck Society for finding. Use of the Stanford Synchrotron Radiation Lightsource, SLAC National Accelerator Laboratory, was supported by the U.S. Department of Energy, Office of Science, Office of Basic Energy Sciences under Contract No. DE-AC02-76SF00515. C.V.S. and S.D. gratefully acknowledge Matthew Latimer for his support and assistance during XAS measurements at beamline 9-3. NRVS data collection was supported by the proposal at BL09XU [2019A1201] at SPring-8. We acknowledge DESY (Hamburg, Germany), a member of the Helmholtz Association HGF, for the provision of experimental facilities. Parts of this research were carried out at Petra III and we would like to thank Dr. Atefeh Jafari for assistance in using P01. Beamtime was allocated for proposal I-20200452. Dr. Jean-Pierre Oudsen is gratefully acknowledged for assistance in the NRVS data acquisition. We thank Prof. S. P. Cramer for fruitful discussions on NRVS data and Prof. S. Leimkühler for ICP-OES measurements. We are grateful to Dr. Johannes Fritsch for performing preliminary experiments on the HoxG intermediates, and to Dr. Anne Christine Schulz for HypCD sample preparations.

Author Contributions

G.C., S.H., S.F., and O.L. conceived and designed experiments, G.C., S.H., S.F., and J.S. conducted molecular biology experiments; S.H. and G.C. performed sample preparations and

biochemical assays; G.C. performed sample preparation for synchrotron measurements; G.C., S.H., C.K.R., and I.Z. performed and analyzed IR spectroscopic experiments; C.Lo. performed and analyzed EPR measurements; M.K., S.Y. and C.Li. performed and analyzed Mössbauer experiments; G.C., Y.Y. and I.S. acquired and analyzed NRVS data; C.v.S. and S.D. performed and analyzed EXAFS experiments; G.C., S.H., O.L, S.F., I.Z. and P.H. analyzed the data; G.C., S.H., S.F., and O.L wrote the manuscript with input from all co-authors. All authors have given approval to the final version of the manuscript.

Competing financial interests

The authors declare no competing interests.

415 **Table**

416 **Table 1:** Ni and Fe content of the various HoxG intermediates determined by ICP-OES and
417 expressed as fraction per protein.

	Fe/protein[a]	Ni/protein[a]
preHoxG$^{\Delta FeNi}$	0.23 ± 0.03	0.03 ± 0.02
preHoxG$^{\Delta Ni}$	0.95 ± 0.05	0.02 ± 0.03
preHoxG	0.86 ± 0.08	0.77 ± 0.09
mHoxG	0.91 ± 0.06	0.75 ± 0.09

418 [a]Data represent mean values ± s.d. (n=3).

419

Figures

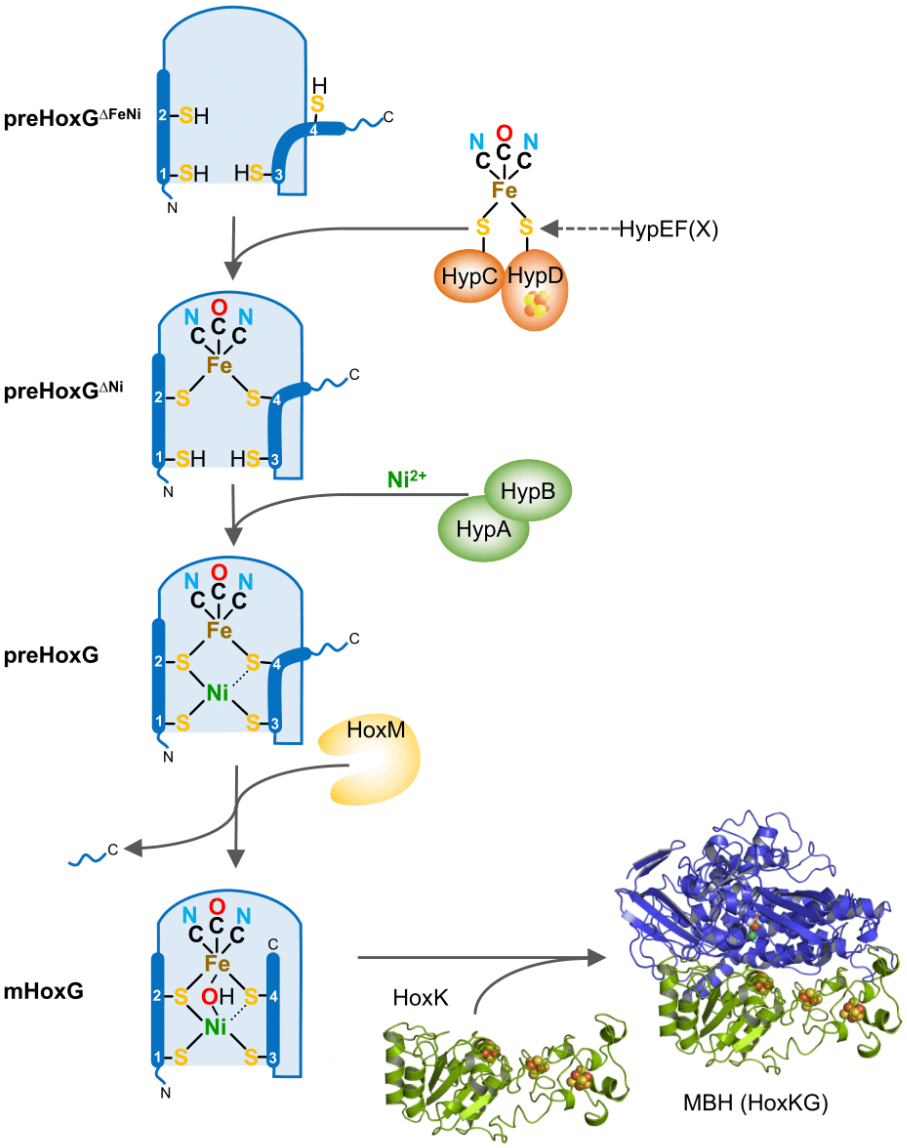

Figure 1: Model of the sequential assembly mechanism of the NiFe(CN)$_2$(CO) center in [NiFe]-hydrogenase. In this study, the maturation intermediates preHoxG$^{\Delta FeNi}$, preHoxG$^{\Delta Ni}$, preHoxG, and mHoxG of the large subunit of the membrane-bound [NiFe]-hydrogenase of *C. necator* were isolated. The fully assembled metal center in mHoxG is coordinated by N-terminal and a C-terminal peptide stretches, each containing two conserved cysteine residues, Cys1/Cys2 and Cys3/Cy4 (white numbers), corresponding to residues Cys75/Cys78 and Cys597/Cys600, respectively, in HoxG.[29] The HoxM protein mediates endoproteolytic removal of the C-terminal extension after incorporation of the [NiFe] center. The PyMOL molecular graphics system (Version 2.2.0) was used to generate cartoon representations of HoxK and MBH.

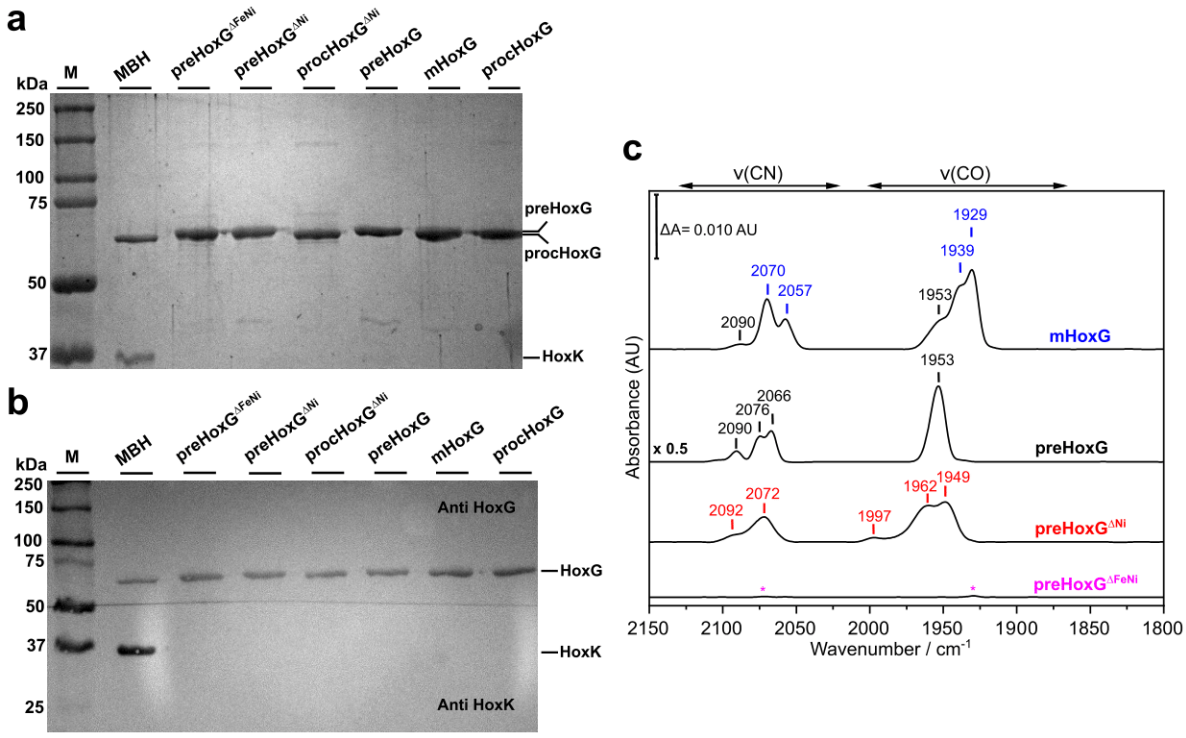

Figure 2: Purification and IR spectroscopic characterization of the HoxG maturation intermediates. The HoxG intermediates were purified via affinity chromatography and separated by SDS-PAGE (0.5 µg per lane) which were **a**) Coomassie-stained or **b**) blotted and treated with antibodies specific for the MBH subunits HoxG and HoxK. Purified native MBH served as control, and the molecular masses of the protein marker (M) are indicated. **c**) Baseline-corrected IR spectra of the HoxG maturation intermediates are displayed in the energy region characteristic for the stretching vibrations of the CO and CN ligands of the hydrogenase active site. The spectra are normalized with respect to the amide II band intensity. Given the narrow bandwidth of the signals of preHoxG, band amplitudes were scaled by a factor of 0.5 for better visualization. Asterisks denote trace CO/CN stretching vibrations in preHoxG$^{\Delta FeNi}$. An enlarged spectrum of these spectral components is shown in **Supplementary Fig. 1**. The IR experiments were performed with three independent samples and yielded consistent results (n=3).

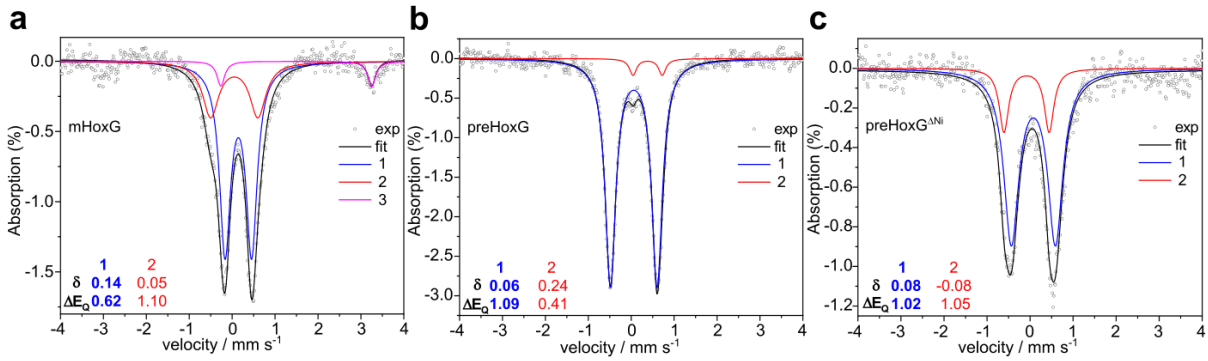

446

447 **Figure 3: Mössbauer spectra of the ^{57}Fe-labeled HoxG maturation intermediates**. The
448 intermediates mHoxG (**a**), preHoxG (**b**) and preHoxG$^{\Delta Ni}$ (**c**) were isolated from $^{57}FeCl_2$-
449 enriched cultures and subjected to Mössbauer spectroscopy (n=1). The experimental raw data
450 and the overall fits are shown in black. The sub-components of the fits are colored in blue (main
451 component) and red (minor component). Minor contributions (comp 3), from high-spin Fe^{II}
452 species in mHoxG are shown in magenta. The isomer shift (δ) and quadrupole splitting (ΔE_Q)
453 parameters in units mm/s are shown in the lower left corner of each graph and listed in
454 **Supplementary Table 3**.
455

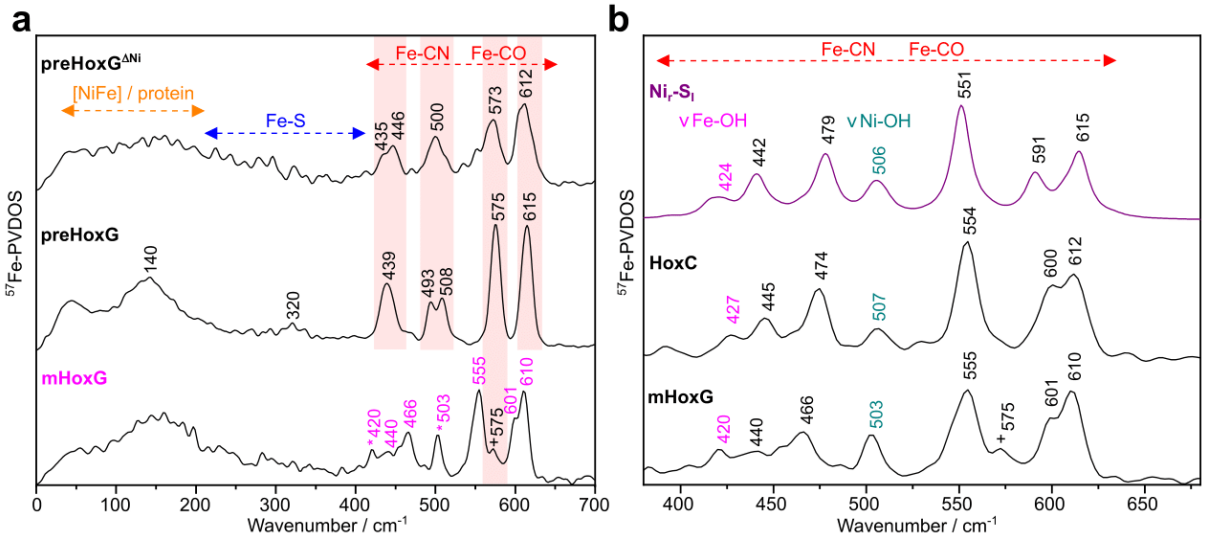

Figure 4: NRVS of ^{57}Fe-labeled HoxG maturation intermediates. a) NRVS partial vibrational density of states (PVDOS) of as-isolated ^{57}Fe-labeled mHoxG (bottom), preHoxG (middle), and preHoxG$^{\Delta Ni}$ (top), normalized to an integrated PVDOS of 3. Different spectral regions are indicated by arrows using the following color code: red, bands related to the Fe–CO/CN moiety of the [NiFe]-active site; orange, bands related to the [NiFe]-active site displacements and protein-related modes; blue, Fe–S bands related to the active site coordinating cysteine residue(s). The light red bars indicate spectral characteristics occurring in both preHoxG and preHoxG$^{\Delta Ni}$. **b**) NRVS-derived spectra of mHoxG (bottom), HoxC (middle) and DFT-computed spectrum of the active site in the Ni_r-S_I state (top).[39] Different spectral regions are indicated by the following color code: red, bands related to the Fe–CO/CN moiety of the [NiFe]-active site; magenta, Fe–OH stretching (ν) vibration; cyan, Ni–OH stretching (ν) vibration. The band at 575 cm^{-1} in mHoxG ($^{+}$) is attributed to remnants of unprocessed preHoxG, which is consistent with the IR and Mössbauer data. Asterisks (*) denote bands with the most prominent bridging hydroxy group (μOH^{-}) displacements. Prominent bands are labeled with the corresponding wavenumbers. The NRVS data (n=1) including the error bars are presented in **Supplementary Figs. 5**, **6**, **7**.

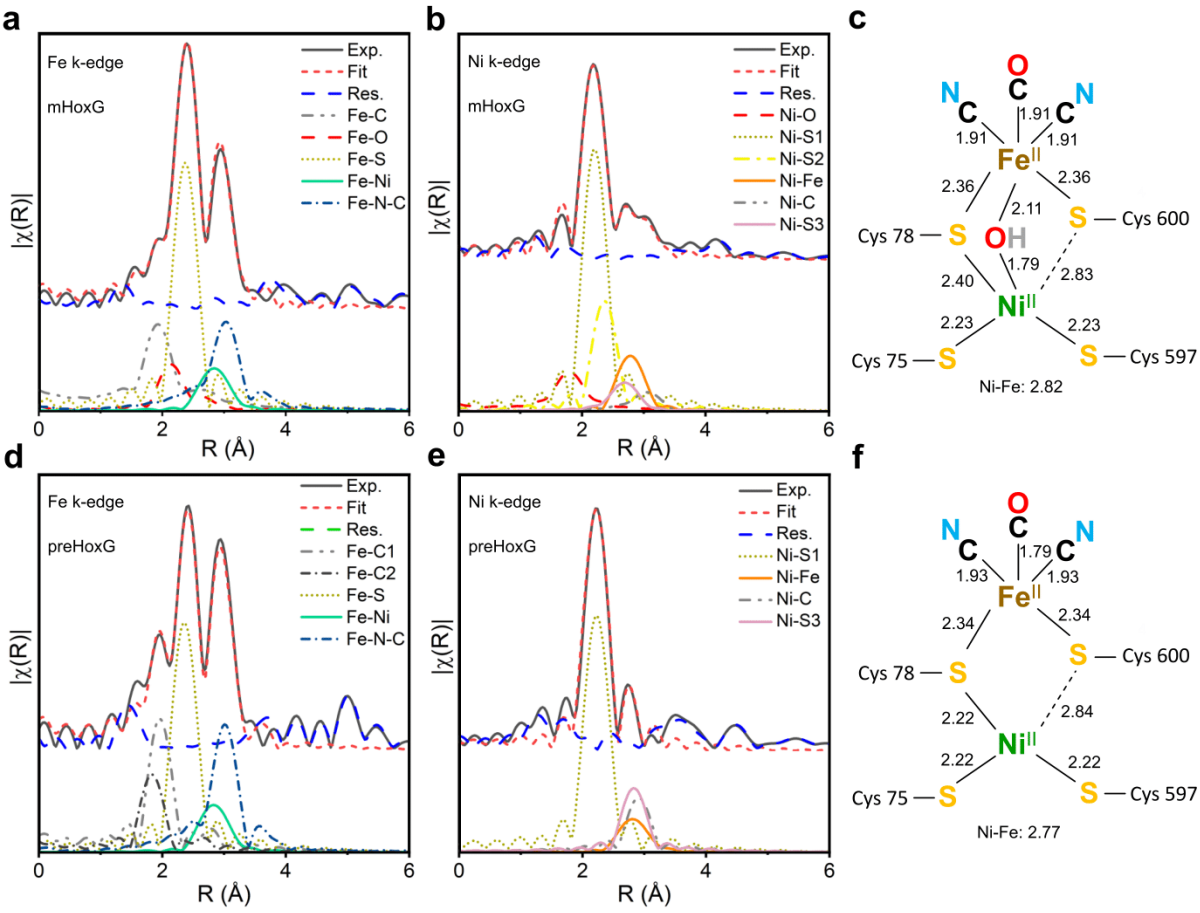

Figure 5: XAS analysis of mHoxG and preHoxG. Panels **a** and **b** show the Fourier-transformed EXAFS spectra (black lines) of the Fe and Ni k-edges of mHoxG, respectively, and panels **d** and **e** show the corresponding spectra of preHoxG (n=1). The overall EXAFS fits for the best fitting models are depicted as dashed red lines, and the individual components are represented as described within the panels. The dashed green line (Res.) represents the difference between the experimental spectra and the fit. The lower panels show the active site models of mHoxG (**c**) and preHoxG (**f**), including the proposed assignment of XAS-derived atom-atom distances. Fourier transform of the presented spectra was performed across a range of k = 3-12 $Å^{-1}$, and modeling was performed across ranges of k = 3-12 $Å^{-1}$ and R = 1-3.2 Å.

References

1. Lubitz, W., Ogata, H., Rüdiger, O. & Reijerse, E. Hydrogenases. *Chem. Rev.* **114**, 4081–4148 (2014).

2. Peters, J. W. *et al.* [FeFe]- and [NiFe]-hydrogenase diversity, mechanism, and maturation. *Biochim. Biophys. Acta* **1853**, 1350–1369 (2015).

3. Vignais, P. M. & Billoud, B. Occurrence, classification, and biological function of hydrogenases: An overview. *Chem. Rev.* **107**, 4206–4272 (2007).

4. Britt, R. D., Rao, G. & Tao, L. Biosynthesis of the catalytic H-cluster of [FeFe] hydrogenase: the roles of the Fe–S maturase proteins HydE, HydF, and HydG. *Chem. Sci.* **11**, 10313–10323 (2020).

5. Shima, S., Fujishiro, T. & Ermler, U. 6 Structure and function of [Fe]-hydrogenase and biosynthesis of the FeGP cofactor. in *Biohydrogen* (ed. Rögner, M.) 127–144 (DE GRUYTER, 2015). doi:10.1515/9783110336733.127.

6. Böck, A., King, P. W., Blokesch, M. & Posewitz, M. C. Maturation of hydrogenases. in *Advances in Microbial Physiology* vol. 51 1–225 (Elsevier, 2006).

7. Lacasse, M. J. & Zamble, D. B. [NiFe]-Hydrogenase Maturation. *Biochemistry* **55**, 1689–1701 (2016).

8. Britt, R. D., Rao, G. & Tao, L. Bioassembly of complex iron–sulfur enzymes: hydrogenases and nitrogenases. *Nat. Rev. Chem.* **4**, 542–549 (2020).

9. Fritsch, J., Lenz, O. & Friedrich, B. Structure, function and biosynthesis of O_2-tolerant hydrogenases. *Nat. Rev. Microbiol.* **11**, 106–114 (2013).

10. Caserta, G. *et al.* Unusual structures and unknown roles of FeS clusters in metalloenzymes seen from a resonance Raman spectroscopic perspective. *Coord. Chem. Rev.* **452**, 214287 (2022).

11. Marques, M. C. *et al.* The direct role of selenocysteine in [NiFeSe] hydrogenase maturation and catalysis. *Nat. Chem. Biol.* **13**, 544–550 (2017).

12. Pierik, A. J., Roseboom, W., Happe, R. P., Bagley, K. A. & Albracht, S. P. J. Carbon monoxide and cyanide as intrinsic ligands to iron in the active site of [NiFe]-hydrogenases. *J. Biol. Chem.* **274**, 3331–3337 (1999).

512 13. Frielingsdorf, S. *et al.* Reversible [4Fe-3S] cluster morphing in an O_2-tolerant [NiFe] hydrogenase.
513 *Nat. Chem. Biol.* **10**, 378–385 (2014).
514 14. Ogata, H., Nishikawa, K. & Lubitz, W. Hydrogens detected by subatomic resolution protein
515 crystallography in a [NiFe] hydrogenase. *Nature* **520**, 571–574 (2015).
516 15. Miki, K., Atomi, H. & Watanabe, S. Structural insight into [NiFe] hydrogenase maturation by
517 transient complexes between Hyp proteins. *Acc. Chem. Res.* **53**, 875–886 (2020).
518 16. Bürstel, I. *et al.* A Universal scaffold for synthesis of the $Fe(CN)_2(CO)$ moiety of [NiFe]
519 hydrogenase. *J. Biol. Chem.* **287**, 38845–38853 (2012).
520 17. Soboh, B. *et al.* [NiFe]-hydrogenase maturation: Isolation of a HypC-HypD complex carrying
521 diatomic CO and CN^- ligands. *FEBS Lett.* **586**, 3882–3887 (2012).
522 18. Reissmann, S. Taming of a Poison: Biosynthesis of the NiFe-hydrogenase cyanide ligands. *Science*
523 **299**, 1067–1070 (2003).
524 19. Schulz, A.-C. *et al.* Formyltetrahydrofolate decarbonylase synthesizes the active site CO ligand of
525 O_2-tolerant [NiFe] hydrogenase. *J. Am. Chem. Soc.* **142**, 1457–1464 (2020).
526 20. Bürstel, I. *et al.* CO synthesized from the central one-carbon pool as source for the iron carbonyl in
527 O_2-tolerant [NiFe]-hydrogenase. *Proc. Natl. Acad. Sci.* **113**, 14722–14726 (2016).
528 21. Senger, M., Stripp, S. T. & Soboh, B. Proteolytic cleavage orchestrates cofactor insertion and
529 protein assembly in [NiFe]-hydrogenase biosynthesis. *J. Biol. Chem.* **292**, 11670–11681 (2017).
530 22. Stripp, S. T. *et al.* Electron inventory of the iron-sulfur scaffold complex HypCD essential in
531 [NiFe]-hydrogenase cofactor assembly. *Biochem. J.* **478**, 3281–3295 (2021).
532 23. Arlt, C. *et al.* Native mass spectrometry identifies the HybG chaperone as carrier of the
533 $Fe(CN)_2CO$ group during maturation of *E. coli* [NiFe]-hydrogenase 2. *Sci. Rep.* **11**, 24362 (2021).
534 24. Watanabe, S. *et al.* Structural basis of a Ni acquisition cycle for [NiFe] hydrogenase by Ni-
535 metallochaperone HypA and its enhancer. *Proc. Natl. Acad. Sci.* **112**, 7701–7706 (2015).
536 25. Hartmann, S., Frielingsdorf, S., Caserta, G. & Lenz, O. A membrane-bound [NiFe]-hydrogenase
537 large subunit precursor whose C-terminal extension is not essential for cofactor incorporation but
538 guarantees optimal maturation. *MicrobiologyOpen* **9**, 1197–1206 (2020).

539 26. Pinske, C., Thomas, C., Nutschan, K. & Sawers, R. G. Delimiting the function of the C-terminal
540 extension of the *Escherichia coli* [NiFe]-hydrogenase 2 large subunit precursor. *Front. Microbiol.*
541 **10**, (2019).
542 27. Pinske, C. & Sawers, R. G. Anaerobic formate and hydrogen metabolism. *EcoSal Plus* **7**,
543 ecosalplus.ESP-0011-2016 (2016).
544 28. Blokesch, M. & Böck, A. Maturation of [NiFe]-hydrogenases in *Escherichia coli*: The HypC
545 cycle. *J. Mol. Biol.* **324**, 287–296 (2002).
546 29. Fritsch, J. *et al.* The crystal structure of an oxygen-tolerant hydrogenase uncovers a novel iron-
547 sulphur centre. *Nature* **479**, 249–252 (2011).
548 30. Lenz, O., Lauterbach, L., Frielingsdorf, S., & Friedrich, B. Oxygen-tolerant hydrogenases and
549 their biotechnological potential. In *Biohydrogen* (M. Rögner (Ed.)) pp. 61–88. (Walter de Gruyter
550 GmbH & Co. KG, 2015).
551 31. Vincent, K. A. *et al.* Electrocatalytic hydrogen oxidation by an enzyme at high carbon monoxide
552 or oxygen levels. *Proc. Natl. Acad. Sci.* **102**, 16951–16954 (2005).
553 32. Hartmann, S. *et al.* O_2-tolerant H_2 activation by an isolated large subunit of a [NiFe] hydrogenase.
554 *Biochemistry* **57**, 5339–5349 (2018).
555 33. Caserta, G. *et al.* The large subunit of the regulatory [NiFe]-hydrogenase from *Ralstonia eutropha*
556 – A minimal hydrogenase? *Chem. Sci.* **11**, 5453−5465 (2020).
557 34. Eberz, G., Eitinger, T. & Friedrich, B. Genetic determinants of a nickel-specific transport system
558 are part of the plasmid-encoded hydrogenase gene cluster in *Alcaligenes eutrophus*. *J. Bacteriol.*
559 **171**, 1340–1345 (1989).
560 35. Bernhard, M., Schwartz, E., Rietdorf, J. & Friedrich, B. The *Alcaligenes eutrophus* membrane-
561 bound hydrogenase gene locus encodes functions involved in maturation and electron transport
562 coupling. *J. Bacteriol.* **178**, 4522–4529 (1996).
563 36. Rossmann, R., Sauter, M., Lottspeich, F. & Böck, A. Maturation of the large subunit (HYCE) of
564 *Escherichia coli* hydrogenase 3 requires nickel incorporation followed by C-terminal processing at
565 Arg537. *Eur. J. Biochem.* **220**, 377–384 (1994).

566 37. Kwon, S. *et al.* Crystal structures of a [NiFe] hydrogenase large subunit HyhL in an immature state
567 in complex with a Ni chaperone HypA. *Proc. Natl. Acad. Sci.* **115**, 7045–7050 (2018).
568 38. Roncaroli, F. *et al.* Cofactor composition and function of a H_2-sensing regulatory hydrogenase as
569 revealed by Mössbauer and EPR spectroscopy. *Chem. Sci.* **6**, 4495–4507 (2015).
570 39. Caserta, G. *et al.* Hydroxy-bridged resting states of a [NiFe]-hydrogenase unraveled by cryogenic
571 vibrational spectroscopy and DFT computations. *Chem. Sci.* **12**, 2189–2197 (2021).
572 40. Caserta, G. *et al. In Vitro* assembly as a tool to investigate catalytic intermediates of [NiFe]-
573 hydrogenase. *ACS Catal.* **10,** 13890–13894 (2020).
574 41. Ogata, H. *et al.* Hydride bridge in [NiFe]-hydrogenase observed by nuclear resonance vibrational
575 spectroscopy. *Nat. Commun.* **6**, 7890 (2015).
576 42. Lorent, C. *et al.* Exploring structure and function of redox intermediates in [NiFe]-hydrogenases
577 by an advanced experimental approach for solvated, lyophilized and crystallized metalloenzymes.
578 *Angew. Chem. Int. Ed.* **60**, 15854–15862 (2021).
579 43. Krämer, T., Kampa, M., Lubitz, W., van Gastel, M. & Neese, F. Theoretical spectroscopy of the
580 Ni^{II} intermediate states in the catalytic cycle and the activation of [NiFe] hydrogenases.
581 *ChemBioChem* **14**, 1898–1905 (2013).
582 44. Blokesch, M. & Böck, A. Properties of the [NiFe]-hydrogenase maturation protein HypD. *FEBS*
583 *Lett.* **580**, 4065–4068 (2006).
584 45. Albareda, M., Pacios, L. F. & Palacios, J. M. Computational analyses, molecular dynamics, and
585 mutagenesis studies of unprocessed form of [NiFe] hydrogenase reveal the role of disorder for
586 efficient enzyme maturation. *Biochim. Biophys. Acta - Bioenerg.* **1860**, 325–340 (2019).
587 46. Magalon, A. & Böck, A. Analysis of the HypC-HycE complex, a key intermediate in the assembly
588 of the metal center of the *Escherichia coli* hydrogenase 3. *J. Biol. Chem.* **275**, 21114–21120 (2000).
589 47. Massanz, C. & Friedrich, B. Amino acid replacements at the H_2-activating site of the NAD-
590 reducing hydrogenase from *Alcaligenes eutrophus*. *Biochemistry* **38**, 14330–14337 (1999).
591 48. Winter, G., Buhrke, T., Jones, A. K. & Friedrich, B. The role of the active site-coordinating
592 cysteine residues in the maturation of the H_2-sensing [NiFe] hydrogenase from *Ralstonia eutropha*
593 H16. *Arch. Microbiol.* **182**, (2004).

49. Esselborn, J. *et al.* Spontaneous activation of [FeFe]-hydrogenases by an inorganic [2Fe] active site mimic. *Nat. Chem. Biol.* **9**, 607–609 (2013).

50. Shima, S. *et al.* Reconstitution of [Fe]-hydrogenase using model complexes. *Nat. Chem.* **7**, 995–1002 (2015).

Methods

Construction of knock-out and expression plasmids.

All bacterial strains, plasmids, and primers used in this study are listed in **Supplementary Table 1**. Plasmid pJH5536, which was used to knock-out the *hoxK* and *hoxG* genes simultaneously was constructed as follows. Plasmid pJH5415[13] was cut with BclI, introducing a deletion of 1913 bp in the *hoxK* and *hoxG* genes, resulting in the fusion of the first 183 codons of *hoxK* with the last 174 codons of *hoxG*. A 1684-bp PstI/XbaI fragment was transferred from the resulting plasmid pJH5513 to a 4862-bp fragment of pLO3,[51] yielding pJH5536.

The plasmids pJH5415 and pSF8.14, harboring the $hoxK_{Strep}$-hoxG and $hoxK_{Strep}$-$hoxG_{proc}$ (*hoxG* lacking the last 15 codons[25]) genes under control of the MBH promoter, served as the basis for the construction of the expression plasmids pGC50 and pGC27, respectively. Using primers GC2 and GC3 (**Supplementary Table 1**), we removed the $hoxK_{Strep}$ genes from both plasmids by Gibson assembly[52] and simultaneously fused a Strep-tag II-encoding sequence to the 5' end of the *hoxG* alleles. Primer GC2 contained the ATG start codon and the Strep-tag II-encoding sequence followed by the initial nucleotides of *hoxG*. The sequence of primer GC3 partly reverse-complemented the GC2 sequence and contained parts of the nucleotide sequence of the MBH (P_{MBH}) promoter region. The fragments resulting from the Gibson assembly were incubated with DpnI and transformed into DH10B competent cells (Thermo Scientific) to yield pGC15 (from pJH5415) and pGC17 (from pSF8.14). The PCR-amplified DNA was checked for accuracy by sequencing. Subsequently, pGC15 and pGC17 were digested with XbaI and SpeI, and the resulting *hoxG*-containing fragments were inserted into XbaI/SpeI-cut pEDY309, yielding pGC50 and pGC27, respectively. APE (A-Plasmid-Editor) was used to plan cloning strategies (https://jorgensen.biology.utah.edu/wayned/ape/.).[53]

Bacterial strains and cultivation

Recombinant *C. necator* strains carrying plasmids for overproduction of HoxG maturation intermediates were constructed as described in the Supplementary Note (**Supplementary Table 1**) and cultivated in a basic mineral medium containing fructose and glycerol as the carbon and energy sources.[54] For isolation of nickel-free HoxG intermediates, the growth medium contained high-purity $FeCl_3$ (>99.99 %), and $NiCl_2$ was omitted. Mineral medium for the production of ^{57}Fe-labeled HoxG intermediates contained $^{57}FeCl_2$ as iron source. When the bacterial cultures reached an optical density at 436 nm of 11-13, the cells were harvested by centrifugation (11,500 x *g*, 4 °C, 15 min), and the cell pellet was flash frozen in liquid nitrogen

and stored at –80 °C until further use. Unique biological materials can be obtained from the authors upon reasonable request.

Protein purification

Native MBH of *C. necator* was purified as described before.[54] Cell pellets of recombinant strains producing the HoxG intermediates were resuspended in lysis buffer (5 mL of buffer per g wet cell paste) consisting of 50 mM K_iPO_4, pH 7.4, 150 mM NaCl, protease inhibitor cocktail (cOmplete EDTA-free, Roche) and DNase I (Roche). The cells were subsequently disrupted in a French pressure cell (G. Heinemann Ultraschall and Labortechnik, Schwäbisch Gmünd, Germany) at 125 MPa. Crude extracts were ultracentrifuged for 40 min at 100,000 x *g* and 4 °C, and the resulting soluble extract was loaded onto a Strep-Tactin® high-capacity column (IBA, Göttingen, Germany). The column was washed with ten bed volumes of washing buffer (50 mM K_iPO_4, pH 7.4, 150 mM NaCl), and the proteins were eluted with 4 bed volumes of washing buffer containing 3 mM D-desthiobiotin. The eluted proteins were concentrated by ultrafiltration (4,000 x *g*, 4 °C) using Amicon Ultracel concentrators (Millipore) with a 30 kDa cut-off. The resulting protein solution was diluted 20-fold with washing buffer and again re-concentrated by ultrafiltration. The final concentrate was flash-frozen and stored in liquid nitrogen. ^{57}Fe-enriched samples were additionally subjected to size-exclusion chromatography on a Superdex 200 Increase 10/300 GL (Cytiva) to reduce nonspecifically bound $Fe^{III/II}$ species copurifying with HoxG intermediates. The protein concentration was determined using a Pierce BCA Protein Assay kit (Thermo Scientific) using bovine serum albumin (BSA) as standard. Data were recorded using the SoftMax Pro 7.0.3 software (Molecular Devices). The protein purity was assessed by SDS-PAGE and Western blot analyses (FluorChem FC2 software, version 3.2.2, Cell Biosciences) using specific antibodies against the MBH subunits HoxG (AK88, 1:10,000) and HoxK (AK87, 1:5000).[35] Alkaline phosphatase-labelled goat-anti-rabbit IgG (Dianova/Jackson ImmunoResearch, product code nr.: 111-055-003, Lot 85152), Hamburg, Germany) was used as secondary antibody (1:10,000).

Metal content analysis

The nickel and iron content of all purified HoxG maturation intermediates was determined by inductively coupled plasma optical emission spectrometry (ICP-OES Optima 2100, Perkin Elmer). A 500 µL sample of 10 µM protein was mixed with 500 µL of ultrapure nitric acid (65 % (v/v)) and incinerated overnight at 100 °C. The sample was then made up to 5 mL with ultrapure H_2O and analyzed for metal content. All measurements were performed in triplicate.

Spectroscopy

Infrared spectroscopy. Protein solutions (0.5-1.0 mM) were transferred into a homemade, gas-tight, and temperature-controlled (10 °C) transmission cell equipped with two sandwiched CaF_2 windows separated by a Teflon spacer (optical pathlength of 50 µm). Spectra with a resolution of 2 cm^{-1} were recorded using a Tensor 27 Fourier-Transform spectrometer (Bruker) equipped with a liquid nitrogen-cooled mercury-cadmium-telluride (MCT) detector. The cell compartment was purged with dried air. For a single spectrum 200 individual scans were averaged. A buffer spectrum was used as reference to calculate the corresponding absorbance spectra. Bruker OPUS software version 7.5 was used for data analysis. For redox treatment of protein samples, sodium dithionite ($Na_2S_2O_4$) and potassium ferricyanide ($K_3Fe(CN)_6$) were used as reducing and oxidizing agents, respectively.

Electron Paramagnetic Resonance spectroscopy. The protein solutions with a volume of 50-100 µL in a concentration range of 0.5-1.0 mM were transferred to quartz EPR tubes (4 mm diameter), frozen in cold ethanol (193 K) and stored in liquid nitrogen for further analysis. A Bruker EMXplus spectrometer equipped with an ER 4122 SHQE resonator, an Oxford EPR 900 helium flow cryostat and an Oxford ITC4 temperature controller was used for EPR measurements. The baseline correction of the experimental spectra was done by subtracting a spectrum of buffer solution measured with the same parameters. If necessary, the spectra were additionally corrected by using a polynomial or spline function. Unless otherwise noted, the following experimental parameters were used: 1 mW microwave power, 9.29 GHz microwave frequency, 10 G modulation amplitude, and 100 kHz modulation frequency. Spectra simulation was performed with the Matlab toolbox Easyspin 5.2.25.[55]

Mössbauer spectroscopy. Zero-field Mössbauer spectra of ^{57}Fe-labeled protein samples at a concentration of 1-1.5 mM were acquired on a SEECO MS6 spectrometer comprising the following instruments: a JANIS CCS-850 cryostat, including a CTI-CRYOGENICS closed cycle 10 K refrigerator, and a CTI-CRYOGENICS 8200 helium compressor. The cold head and sample mount were equipped with calibrated DT-670-Cu-1.4L silicon diode temperature probes and heaters. Temperature was controlled by a LAKESHORE 335 temperature controller. Spectra were recorded using an LND-45431 Kr gas proportional counter with beryllium window connected to the SEECO W204 γ-ray spectrometer that includes a high voltage supply, a 10 bit and 5 µs ADC and two single channel analyzers. Motor control and recording of spectra were taken care of by the W304 resonant γ-ray spectrometer. For the reported spectra a RIVERTEC MCO7.114 source (^{57}Co in Rh matrix) with an activity of about 1 GBq was used.

All spectra were recorded on frozen solutions at 13 K, and data were accumulated for about 24-72 hours. Mössbauer data were processed and simulated using the WMOSS4 program (www.wmoss.org). Isomeric shifts are referenced to α-iron at room temperature.

X-ray absorption spectroscopy. Samples of mHoxG and preHoxG proteins were purified as described above and concentrated to 2.0 mM in 50 mM K_iPO_4, pH 7.4, 150 mM NaCl. XAS measurements were performed at beamline 9–3 of the Stanford Synchrotron Radiation Lightsource (SSRL). The SPEAR storage ring operated at 3.0 GeV in top-off mode with a ~500 mA ring current. A liquid N_2-cooled double-crystal monochromator with Si(220) crystals (ϕ = 0°) was used to select incident X-ray energies with an intrinsic resolution ($\Delta E/E$) of ~0.6×10^{-4}, and a Rh-coated mirror was used for harmonic rejection. The X-ray beam size was 1 × 4 mm^2 (V × H) at the sample position. An inert 20 K sample environment was maintained using a liquid helium flow cryostat minimize radiation damage and sample degradation, and fluorescence measurements were collected using a Canberra 100-element Ge monolith solid-state detector. Each sample was checked for signs of radiation damage prior to measurement by performing subsequent scans (five minutes each) over the same sample spot. These tests showed both mHoxG and preHoxG proteins were stable under X-ray irradiation at either Ni or Fe K-edge for up to 20 minutes. The energy of incoming X-rays was calibrated by simultaneous measurement of metal foil and assignment of the first inflection to 8333.0 eV for Ni, and 7111.2 eV for Fe. Full XAS scans at Ni were collected by scanning the incident energy from 8103 to 9328 eV, while full Fe XAS scans were collected by from 6882 to 8126 eV. XAS data were processed using Athena, part of the Demeter software package (https://bruceravel.github.io/demeter/). Theoretical EXAFS models were calculated using Artemis by using the multiple scattering FEFF6 code.

Nuclear resonance vibrational spectroscopy. NRVS measurements were conducted at SPring-8 BL09XU (Japan) and Petra III P01 (Germany) with fluxes of ~$2.8 \cdot 10^9$ and ~$6.4 \cdot 10^9$ photons/s, respectively, using 14.41 keV radiation (^{57}Fe). The experimental setup at both beamlines comprises a two-step monochromatization of the beam (energy resolution of 0.8 meV at BL09XU and 1.0 meV at P01) and detection of the delayed nuclear fluorescence and the Kα fluorescence following nuclear excitation by avalanche photo diodes.[56] Raw NRVS data were converted to single-phonon ^{57}Fe partial vibrational densities of states (PVDOS) using the PHOENIX software package via the "NRVS Spectra Processing Tool" web interface (https://www.spectra.tools/).[57,58] The energy scales were calibrated with a $[NEt_4][^{57}FeCl_4]$ sample characterized by two prominent peaks at 378 cm^{-1} (asymmetric Fe–Cl stretching mode), and 139 cm^{-1} (Fe–Cl bending mode) (**Supplementary Fig. 14**). The temperature of the samples

731 was maintained at ca 12 K using a LHe cryostat. The Stoke/anti-Stoke imbalance-derived real
732 sample temperatures were 15-50 K.[59] To emphasize the region of interest, sectional
733 measurements of the spectral regions were performed. Each scan was divided into segments
734 with different data collection times (second per point, s/pt). We used 3-4 s/pt for the region
735 from -80 to 360 cm^{-1} and 9-10 s/pt for the region from 360 to 700 cm^{-1}.

736

Data availability

The authors declare that the data supporting the findings of this study are available within the article and the Supplementary Information. Source data are provided with this paper. Raw XAS data were obtained at the SSRL synchrotron. Raw NRVS data were generated at the synchrotron facilities Petra III and SPring-8, and are available in their processed form upon request. Additional reagents will be made available by the corresponding authors upon reasonable request.

Methods-only references

51. Lenz, O. & Friedrich, B. A novel multicomponent regulatory system mediates H_2 sensing in *Alcaligenes eutrophus*. *Proc. Natl. Acad. Sci.* **95**, 12474–12479 (1998).

52. Gibson, D. G. *et al.* Enzymatic assembly of DNA molecules up to several hundred kilobases. *Nat. Methods* **6**, 343–345 (2009).

53. Davis, M. W. & Jorgensen, E. M. ApE, A Plasmid Editor: A Freely Available DNA Manipulation and Visualization Program. *Front. Bioinforma.* **2**, 818619 (2022).

54. Lenz, O., Lauterbach, L. & Frielingsdorf, S. O_2-tolerant [NiFe]-hydrogenases of *Ralstonia eutropha* H16: Physiology, molecular biology, purification, and biochemical analysis. In *Methods in Enzymology* vol. 613 117–151 (Elsevier, 2018).

55. Stoll, S. & Schweiger, A. EasySpin, a comprehensive software package for spectral simulation and analysis in EPR. *J. Magn. Reson.* **178**, 42–55 (2006).

56. Scheidt, W. R., Li, J. & Sage, J. T. What can be learned from nuclear resonance vibrational spectroscopy: Vibrational dynamics and hemes. *Chem. Rev.* **117**, 12532–12563 (2017).

57. Sturhahn, W. CONUSS and PHOENIX: Evaluation of nuclear resonant scattering data. *Hyperfine Interact.* **125**, 149–172 (2000).

58. Gee, L. B., Wang, H. & Cramer, S. P. NRVS for Fe in biology: Experiment and basic interpretation. in *Meth. Enzymol.* vol. 599 409–425 (Elsevier, 2018).

59. Wang, H., Yoda, Y., Kamali, S., Zhou, Z.-H. & Cramer, S. P. Real sample temperature: a critical issue in the experiments of nuclear resonant vibrational spectroscopy on biological samples. *J. Synchrotron Radiat.* **19**, 257–263 (2012).